Supporting Information

1. Experimental

1.1. Preparation of materials

Bismuth nitrate pentahydrate [$Bi(NO_3)_3 \cdot 5H_2O$, 99.0%], anhydrous sodium sulfate (Na_2SO_4, 99.5%), dimethyl sulfoxide (C_2H_6SO, 99.8%), vanadyl acetylacetonate ($VO(acac)_2$, 98%), potassium iodide (KI, AR), p-benzoquinone ($C_6H_4O_2$, 99%), ammonium fluoride (NH_4F, 98%), iron nitrate nonahydrate ($Fe(NO_3)_3 \cdot 9H_2O$, AR), hexahydrate Cobalt nitrate ($Co(NO_3)_2 \cdot 6H_2O$, AR), lanthanum nitrate hexahydrate ($La(NO_3)_2 \cdot 6H_2O$, AR) were purchased from Aladdin Company, absolute ethanol (C_2H_6O, AR), urea ($CO(NH_2)_2$, AR), sodium sulfite (Na_2SO_3, AR), sodium hydroxide (NaOH, AR) were purchased from Sinopharm Chemical Reagent Co., Ltd., and nitric acid (HNO_3, AR) was purchased from Nanjing Chemical Reagent Co., Ltd. In the experiments, all chemicals were used directly without any further purification.

1.2. Preparation of composite photoanodes

1.2.1. Preparation of BiVO$_4$ photoanodes

The $Bi(NO)_3$ solution was prepare by dissolving 0.97 g of $Bi(NO)_3 \cdot 5H_2O$ in 50 mL of KI solution, which contained 3.32 g of KI. The pH of solution was adjusted to ~1.7 by adding HNO_3. This solution was mixed with 20mL of alcohol containing 0.49 g p-benzoquinone. A typical three-electrode system was employed for electrodeposition. A piece of fluorine-doped tin oxide (FTO) glass was used as the working electrode, an Ag/AgCl electrode (filled with 3.3 mol L^{-1} KCl) served as the reference electrode, and platinum foil was employed as the counter electrode.

Electrochemical workstation (CHI-660E, Shanghai Chenhua, China) was used for sample preparation and performance test. Electrodeposition was performed at -0.1 V (vs. Ag/AgCl) for 300s, corresponding to the amount of deposit charge was 0.3 C cm^{-2}. The obtained BiOI precursor was washed by DI water and dried in air naturally. The following is 100 μL of dimethyl sulfoxide solution containing 0.2 M VO (acac)$_2$ was dropped on the surface of BiOI electrode (1×1 cm). Then the electrode was heated in a muffle furnace at 450 °C (ramping rate of 2 °C min^{-1}) for 2 h. Excess V$_2$O$_5$ at the surface of BiVO$_4$ was removed by immersing the electrode in 1 M NaOH for 0.5 h with slow stirring. Finally, the product BiVO$_4$ electrode was washed with DI water and dried in air.

1.2.2. Preparation of Co$_2$Fe$_1$-LDHs/BiVO$_4$ composite photoanodes

Composite photoanodes were prepared using a simple hydrothermal method. 0.1 mmol Co(NO$_3$)$_2$·6 H$_2$O, 0.05 mmol Fe(NO$_3$)$_3$·9H$_2$O, 1.5 mmol urea, 0.375 mmol NH$_4$F were dissolved in 50 mL deionized solution, and stirred vigorously for 30 minutes to form a uniform metal salt solution. 15 mL of precursor solution was placed into a 25 mL Teflon-lined autoclave, and a piece of BiVO$_4$ electrode was put into it while the BiVO$_4$ side was facing down. The mixture was heated at 90 °C for 4 h, and the formed composite was thoroughly washed with DI water and dried at room temperature before using.

1.2.3. Preparation of Co$_2$Fe$_x$La$_{1-x}$-LDHs/BiVO$_4$ composite photoanode

In the preparation process of Co$_2$Fe$_x$La$_{1-x}$ -LDHs, 0.1 mmol Co(NO$_3$)$_2$·6 H$_2$O, 0.01 mmol Fe(NO$_3$)$_3$·9H$_2$O, 0.04 mmol La(NO$_3$)$_3$·6 H$_2$O, 1.2 mmol urea, 0.075 mmol NH$_4$F

were dissolved in 50 mL deionized solution (Co^{2+}:[Fe^{3+}+La^{3+}] =2), and stirred vigorously for 30 minutes to form a uniform metal salt solution. 15 mL of precursor solution was placed into a 25 mL Teflon-lined autoclave, and a piece of $BiVO_4$ electrode was put into it while the $BiVO_4$ side was facing down. The mixture was heated at 90 °C for 4 h, and the formed composite was thoroughly washed with DI water and dried at room temperature before using. The final product was named as $Co_2Fe_{0.2}La_{0.8}$-LDH.

In order to compare the effect of adding La on the OER, this prepared process controlled the ratio of Fe and La in $Co_2Fe_xLa_{1-x}$ -LDHs by adjusting the amount of $Fe(NO_3)_3 \cdot 9H_2O$ and $La(NO_3)_3 \cdot 6H_2O$. Maintaining the total moles of Fe^{3+} and La^{3+} at 0.05 mmol, change the addition amount of $Fe(NO_3)_3 \cdot 9H_2O$ and $La(NO_3)_3 \cdot 6H_2O$, and the products were named as $Co_2Fe_{0.1}La_{0.9}$-LDH, $Co_2Fe_{0.5}La_{0.5}$-LDH and $Co_2Fe_{0.8}La_{0.2}$-LDH.

1.3. Characterizations

The morphology and structure of as-prepared photoanodes were explored by scanning electron microscopy (SEM, Hitachi S-4700) and transmission electron microscopy (TEM, Hitachi 7700), respectively. The distribution of element of as-prepared photoanodes were characterized by the energy-dispersive spectroscopy (EDS, JEOL-6701F). The crystal structure of as-prepared photoanodes were studied on X-ray diffractometer (XRD, D/max-2500 VB2+/PC equipped with Cu-Ka radiation (λ = 0.15406 nm)). The microstructure of as-prepared photoanodes were explored by the High-resolution transmission electron microscopy (HRTEM, Hitachi H-9500). The

chemical states and composition of as-prepared photoanodes were explored by X-ray photoelectron spectroscopy (XPS, Thermo ESCALAB250). The UV–vis diffuse spectra of all photoanodes were performed on the UV-8000S. Electron paramagnetic resonance (EPR) spectra of as-prepared samples were characterized by a low temperature (77K) pulse electron paramagnetic resonance spectrometer. Electron spin resonance (ESR) signals of spin-trapped radicals were detected on a Bruker model ESR JESFA200 spectrometer using spin-trap reagent DMPO. For the operando ESR characterization, 0.5 M sodium sulfate, a platinum electrode, and Ag/AgCl electrode were respectively employed as electrolyte, reference electrode, and counter electrode. After reaction, 30 μL electrolyte was mixed with 30 μL DMPO solution. The solution was drawn into a capillary and placed in a quartz tube, which was then inserted into the EPR resonant cavity to capture free radicals for testing. Photocatalytic H_2-evolution activities from water-splitting of the samples were evaluated by CEL-SPH2N photocatalytic water splitting into H_2 system. 0.1 g of the photocatalyst was dispersed in the mixed solution containing 90 mL of deionized water and 10 mL of methanol (as sacrificial agent), and put in a closed quartz reactor. A 300 W Xe lamp equipped with a cutoff filter of 420 nm was used to provide visible light irradiation (> 420 nm). Before reaction, the reaction system was evacuated to ensure complete removal of air, O_2 and CO_2 gases in the solution by aeration of N_2. Then turning on the light kept photocatalytic water-splitting reaction for 6 h. Evolved-H_2 was analyzed by gas chromatography (Shanghai FanWei Science and Technology Ltd. GC9860, 5A column, TCD, and Ar carrier).

1.4. Photoelectrochemical measurements

All PEC properties measurements were tested on a Zahner electrochemical workstation. The light source is a Xe 300 W lamp with AM 1.5 G filter and the light intensity was calibrated to 100 mW cm^{-2} by a photometer (International Light ILT 1400A). 0.5 M Na$_2$SO$_4$ (pH =7) with or without 0.5 M Na$_2$SO$_3$ solution as hole scavenger was used as the electrolyte. As-prepared photoanodes were illuminated from the non-conductive side of FTO with an irradiation area of 1.0 cm^2. The linear sweep voltammetry (LSV) plots were scanned on the Zahner electrochemical workstation with a sweep potential from -0.6 to 0.8 V (vs. Ag/AgCl) and a scanning rate of 10 mV s^{-1}. According to Nernst equation (Eq. 1), the potential vs. RHE can be calculated from the potential vs. Ag/AgCl.

$$E_{RHE} = E_{Ag/AgCl} + 0.0591 \times pH + E_{Ag/AgCl}^{0} \tag{1}$$

E_{RHE} represents the converted potential versus RHE, while $E_{Ag/AgCl}$ refers to the obtained potential versus Ag/AgCl electrode. The normal potential of Ag/AgCl electrode ($E_{Ag/AgCl}^{0}$) is 0.1976 V at 25°C. Both surface charge injection efficiency ($\eta_{surface}$) and charge separation efficiency (η_{sep}) can be calculated according to Eqs. (2–3).

$$\eta_{Surface}(\%) = \frac{J_{water}}{J_{Na2SO3}} \tag{2}$$

$$\eta_{Sep}(\%) = \frac{J_{Na2SO3}}{J_{abs}} \tag{3}$$

Where J_{water} and J_{Na2SO3} are photocurrent densities of the water oxidation and sulfite oxidation, respectively. Jabs represents the theoretical photocurrent density, which is based on the assumption of that the photons absorbed are completely converted

to the current. In addition, applied bias photon to current efficiency (ABPE) can be calculated according to the LSV curves by Eq. (4):

$$ABPE(\%) = \frac{J \times (1.23 - V_{bias})}{PAM1.5} \times 100\%$$

(4)

Where J is the photocurrent density (mA cm^{-2}) indicated by LSV curves. V_{bias} represents the applied bias versus RHE (V), and PAM 1.5 is 100 mV cm^{-2}. The incident photon-to-current conversion efficiency (IPCE) is calculated based on the determination of photocurrent densities at specific wavelengths using the light source with a monochromator (Eq. 5):

$$IPCE(\%) = \frac{1240 \times J}{\lambda \times P_{light}} \times 100\%$$

(5)

Where P_{light} and J represent the light power density and photocurrent density at a specific wavelength, respectively. And λ refers to incident wavelength. In addition, within the frequency ranges of 0.1–100000 Hz, both photoelectrochemical impedance spectroscopy under AM 1.5 G illumination and electrochemical impedance spectroscopy (EIS) in dark condition were conducted with an AC voltage amplitude of 5mV at the open-circuit potential. Mott-Schottky (MS) measurements were performed at different frequencies (1000 Hz and 500 Hz) using Na_2SO_4 (0.5 M, pH = 9.33) as the electrolyte solution. According to Eq. (6), the charge carrier densities (Nd) can be calculated based on the MS curves measured at 1000 Hz in the dark.

$$N_d = [d(1/C^{\wedge}2)/dV]^{-1}$$

(6)

1.5. Computational details

We have employed the Vienna Ab Initio Package (VASP)[1, 2] to perform all the

spin-polarized density functional theory (DFT) calculations within the generalized gradient approximation (GGA) in the PBE[3] formulation. We have chosen the projected augmented wave (PAW) potentials[4, 5] to describe the ionic cores and take valence electrons into account using a plane wave basis set with a kinetic energy cutoff of 450 eV. Partial occupancies of the Kohn−Sham orbitals were allowed using the Methfessel-Paxton smearing method and a width of 0.10 eV. The electronic energy was considered self-consistent when the energy change was smaller than 10^{-6} eV. A geometry optimization was considered convergent when the residual forces were smaller than 0.05 eV/Å. The free energy of a gas phase molecule or an adsorbate on the surface was calculated by the equation $G = E + ZPE - TS$, where E is the total energy, ZPE is the zero-point energy, T is the temperature in kelvin (298.15 K is set here), and S is the entropy. The transition state of an elementary reaction step was located by the nudged elastic band (NEB) method[6]. In the NEB method, the path between the reactant(s) and product(s) was discretized into a series of structural images. The intermediate images were relaxed until the perpendicular forces were smaller than 0.05 eV/Å.

The four-electron pathway of OER occurs in alkaline aqueous solution was generally reported to proceed according to the following steps.

$* + H_2O \rightarrow *OH + e^- + H^+, \Delta G_1$

$*OH \rightarrow *O + e^- + H^+, \Delta G_2$

$*O + H_2O \rightarrow *OOH + e^- + H^+, \Delta G_3$

$*OOH \rightarrow O_2 + * + e^- + H^+, \Delta G_4$
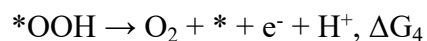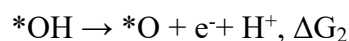
Where "*" represents the active site on the catalyst, and *O, *OH, and *OOH are the intermediates of adsorption. The Gibbs free energy of OER process can be calculated based on adsorption energy of intermediate products (E_{abs}), zero-point energy of reaction (ΔE_{ZPE}) and entropy (ΔS). Herein, ΔU is the energy difference between 0 K and temperature t.

a

b

~1.08μm

FTO

Glass

1 μm
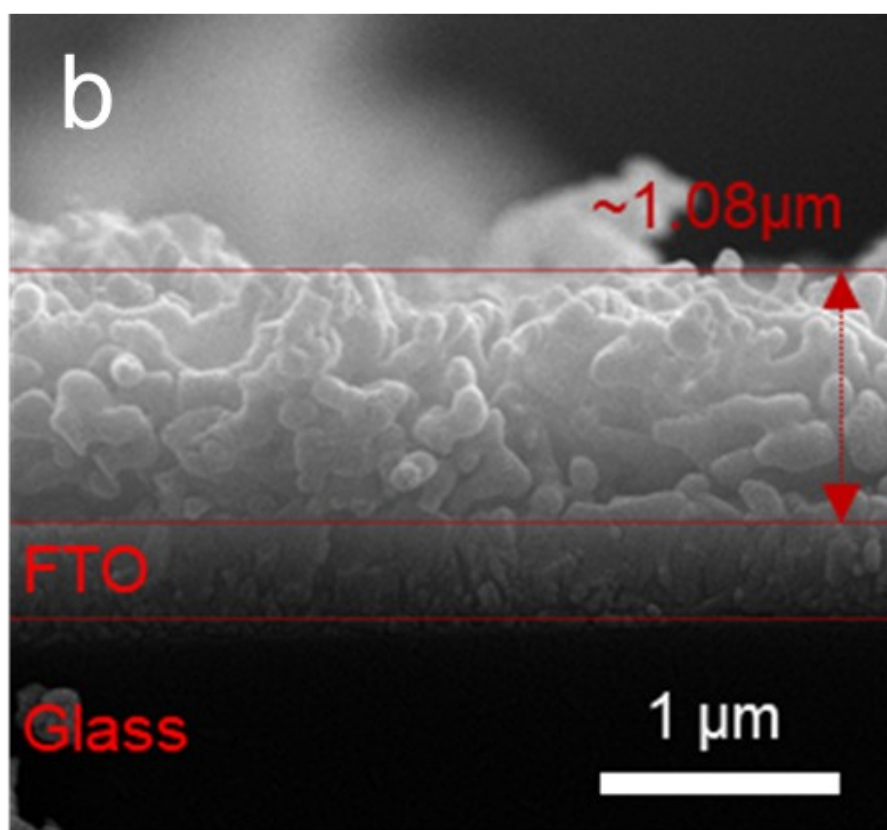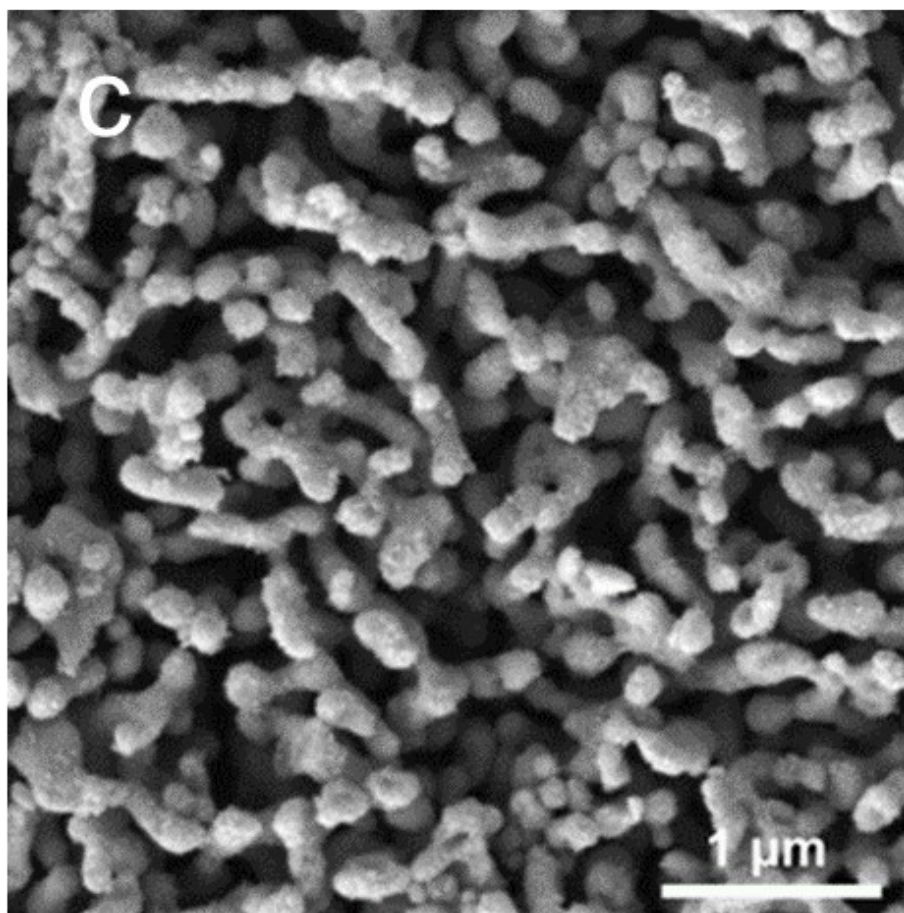
Fig. S1 The SEM images of (a, b) $BiVO_4$ and (c) Co_2Fe_1-LDHs/$BiVO_4$.
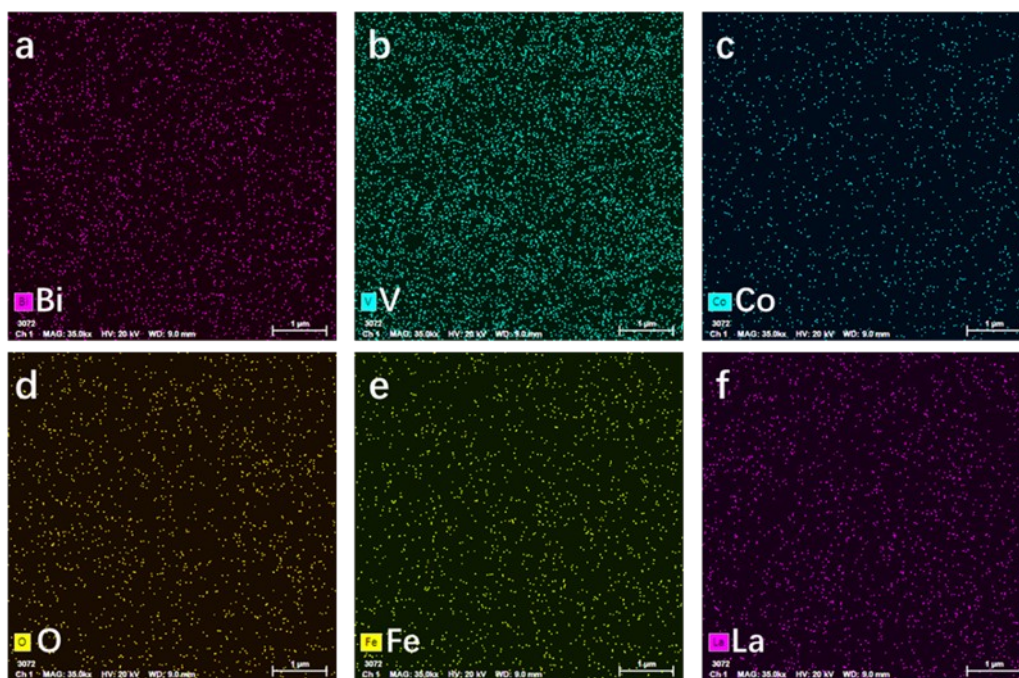
Fig. S2 The corresponding SEM-EDS mapping images of $Co_2Fe_{0.2}La_{0.8}$-LDHs/$BiVO_4$.
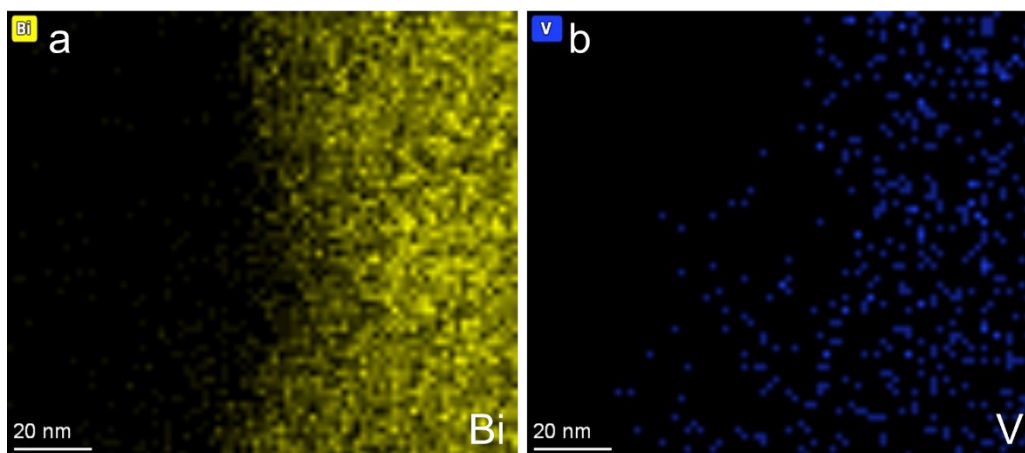
Fig. S3 The corresponding EDS mapping images of $Co_2Fe_{0.2}La_{0.8}$-LDHs/$BiVO_4$.
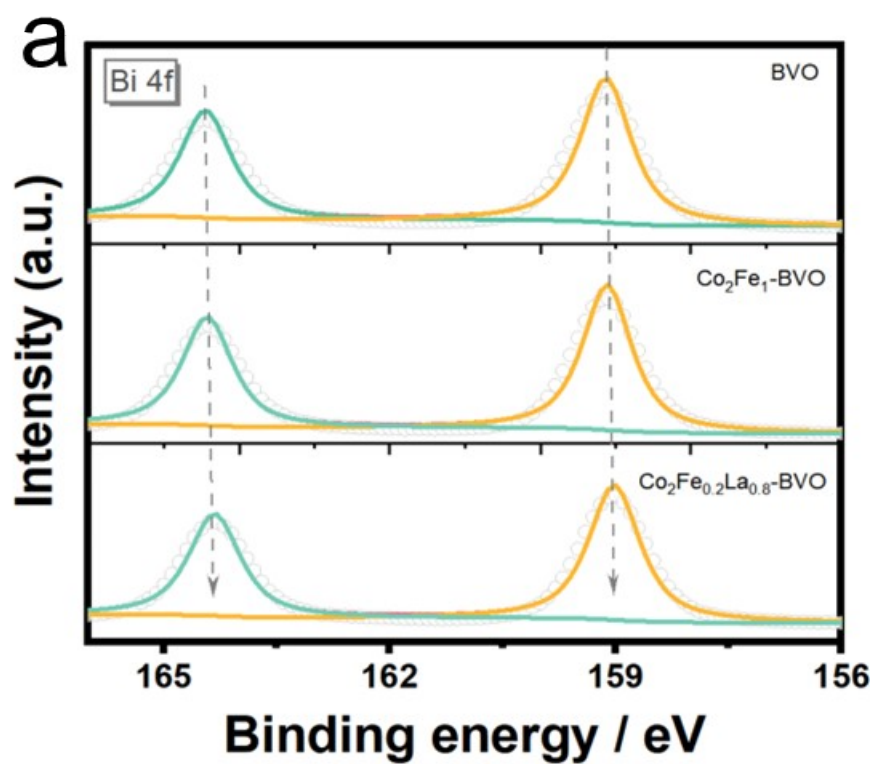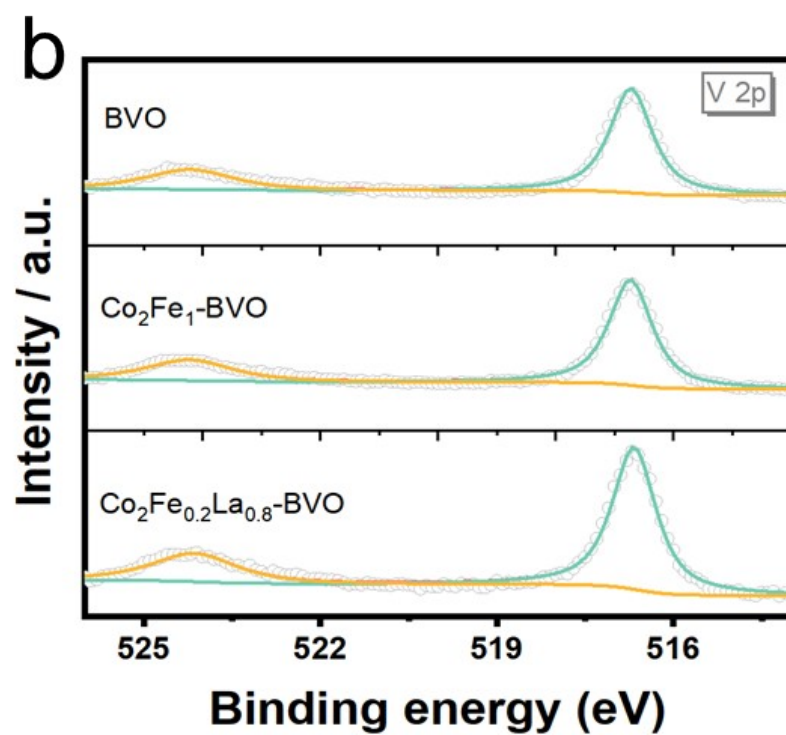
Fig. S4 XPS spectra of $BiVO_4$, Co_2Fe_1-LDHs/$BiVO_4$ and $Co_2Fe_{0.2}La_{0.8}$-LDHs/$BiVO_4$:

(a) Bi 4f, (b) V 2p.
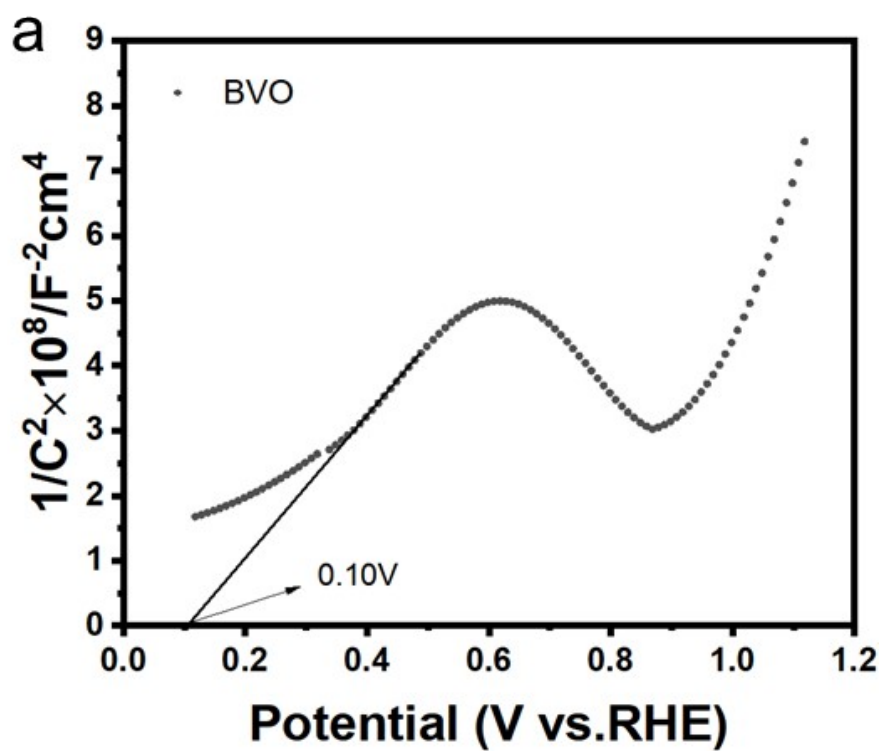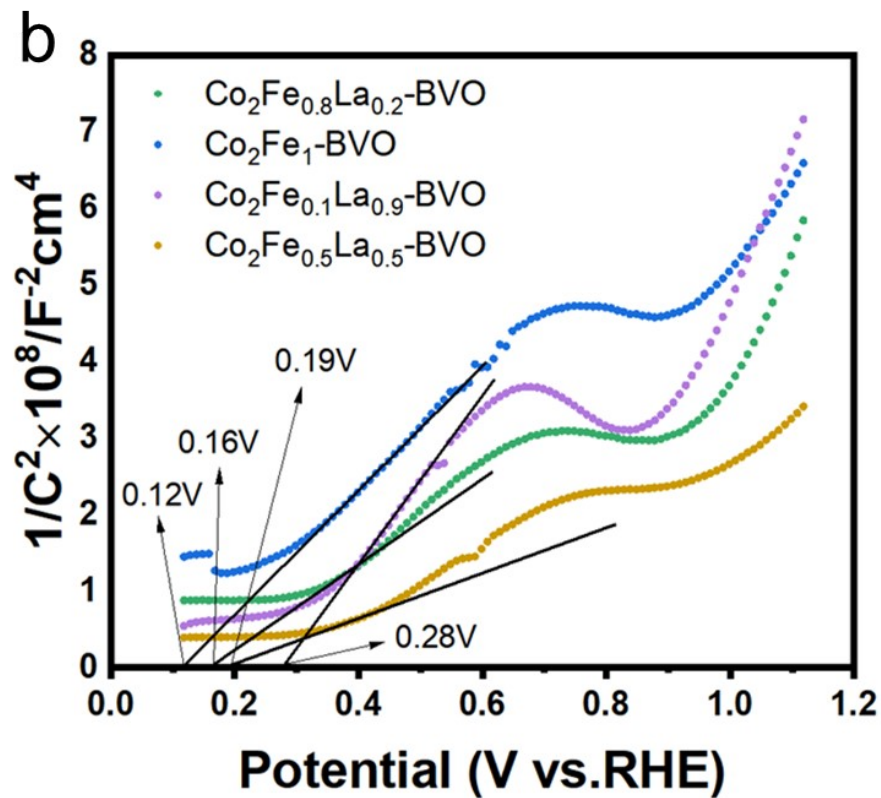
Fig. S5 Mott Schottky (MS) curves of (a) BiVO$_4$, and (b) Co$_2$Fe$_x$La$_{1-x}$-LDHs/BiVO$_4$.
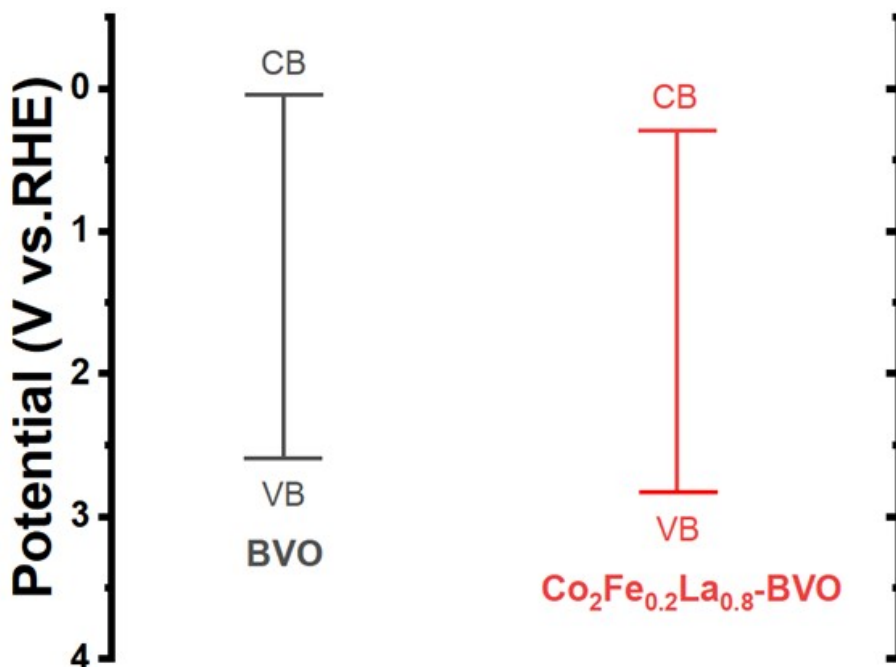
Fig. S6 Band structures of BiVO$_4$ and Co$_2$Fe$_{0.2}$La$_{0.8}$-LDHs/BiVO$_4$.
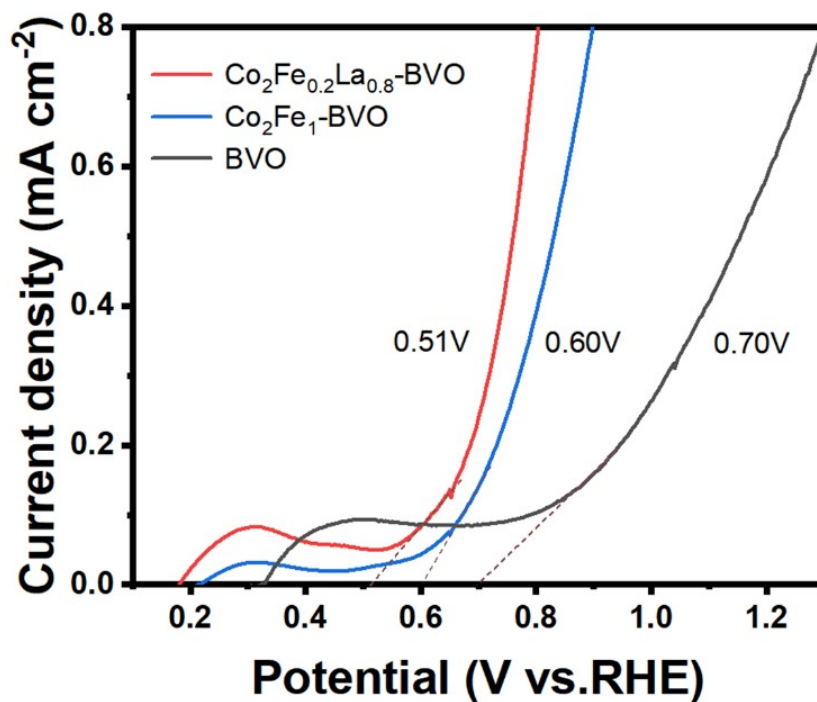
Fig. S7 Onset potentials of $BiVO_4$, Co_2Fe_1-LDHs/$BiVO_4$ and $Co_2Fe_{0.2}La_{0.8}$-LDHs/$BiVO_4$.
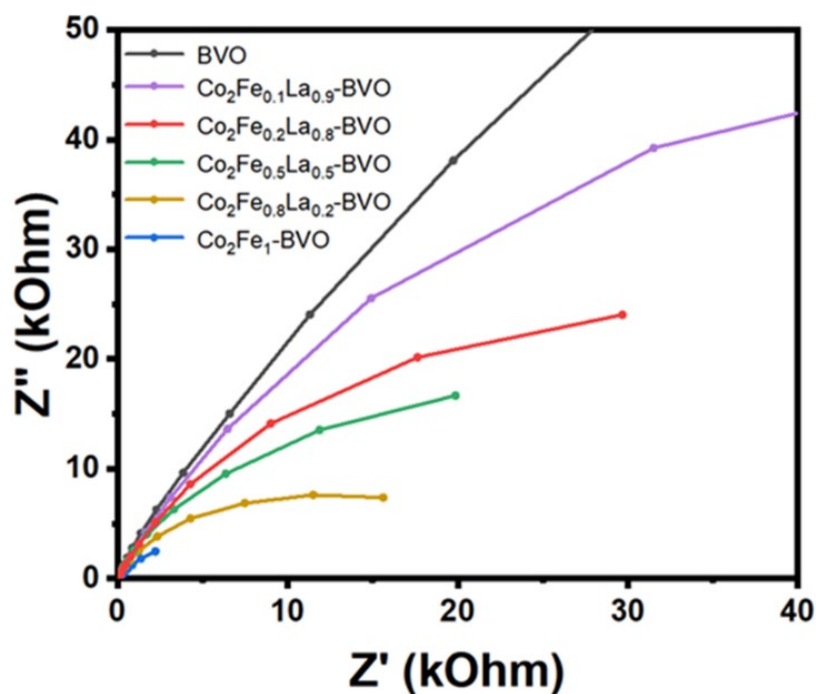
Fig. S8 EIS under dark irradiation of $BiVO_4$, Co_2Fe_1-LDHs/$BiVO_4$ and $Co_2Fe_xLa_{1-x}$-LDHs/$BiVO_4$.
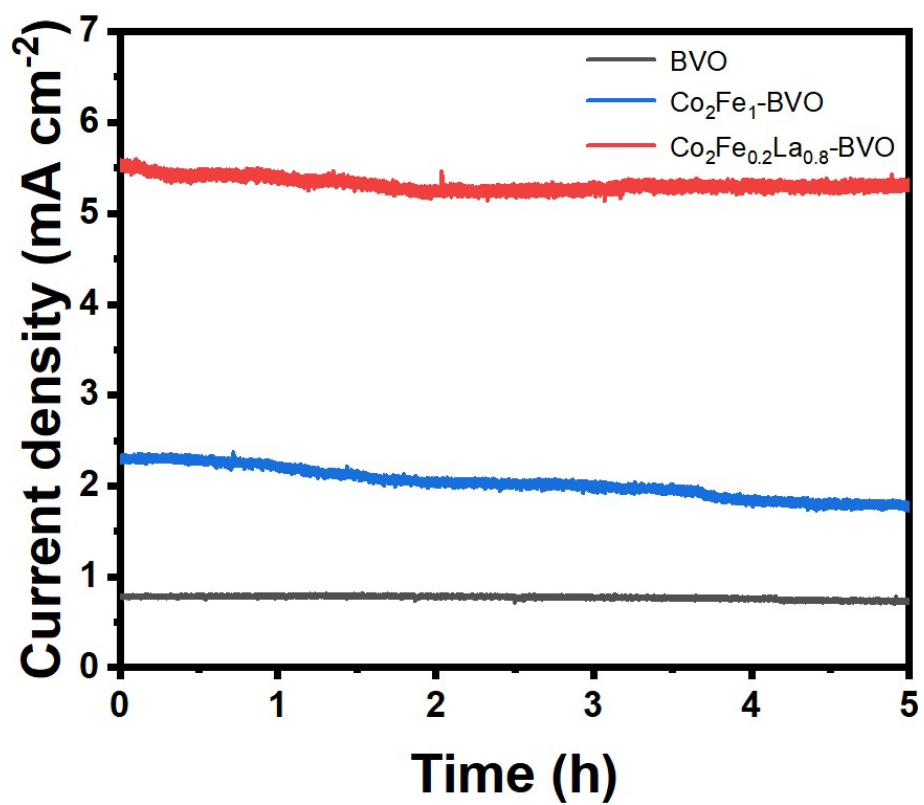
Fig. S9 I-t curves for $BiVO_4$, Co_2Fe_1-LDHs/$BiVO_4$ and $Co_2Fe_{0.2}La_{0.8}$-LDHs/$BiVO_4$ photoanodes under continuous illumination at 0.6 V vs. RHE for 5h.
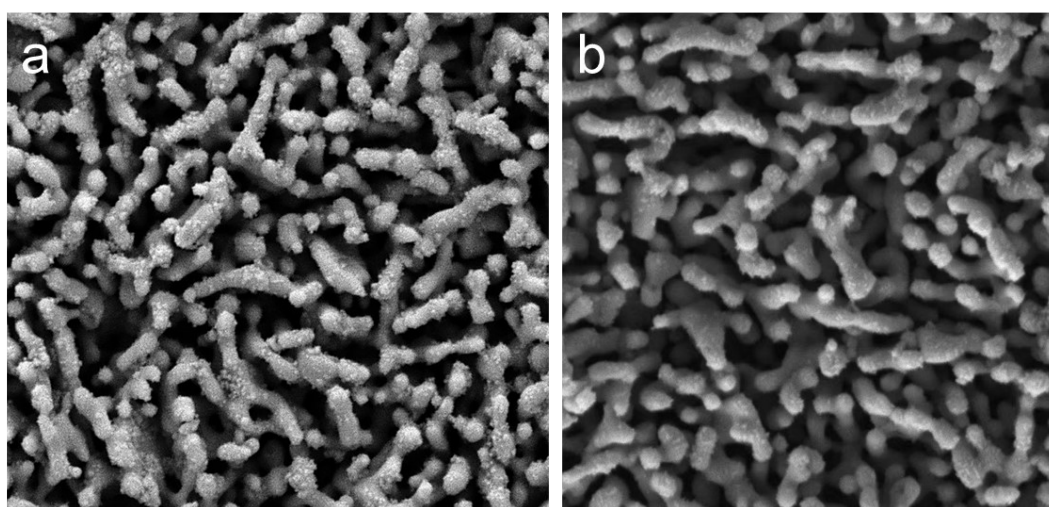
Fig. S10 The SEM images of $Co_2Fe_{0.2}La_{0.8}$-LDHs/$BiVO_4$ catalyst (a) before and (b) after reaction.
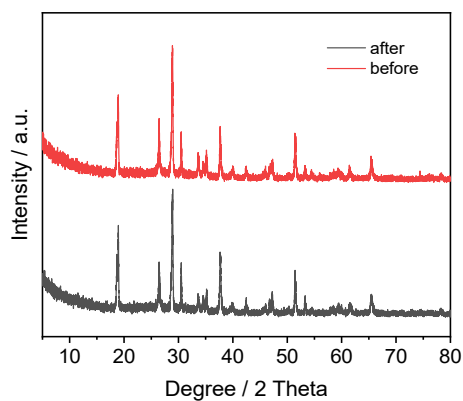
Figure S11. XRD patterns of $Co_2Fe_{0.2}La_{0.8}$-LDHs/$BiVO_4$ catalyst (a) before and (b) after reaction.
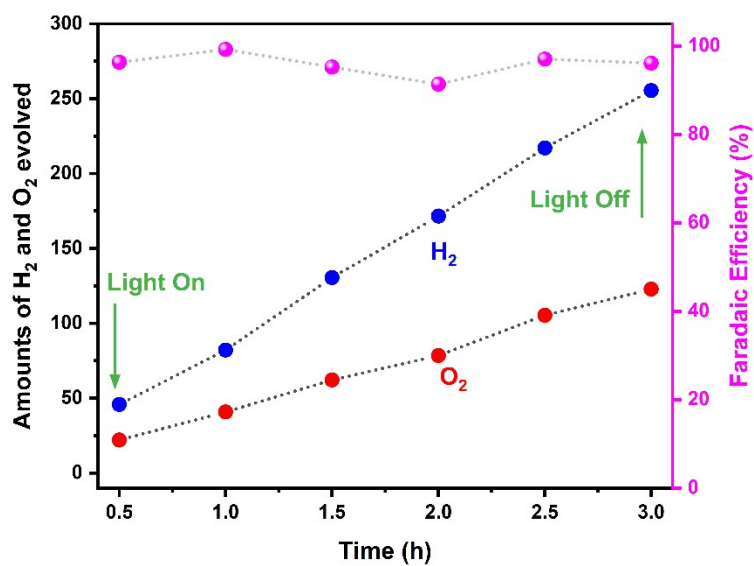
Fig. S12 Evolved H_2/O_2 amounts and FE over time during 3 h on $Co_2Fe_{0.2}La_{0.8}$-LDHs/$BiVO_4$ photoanode
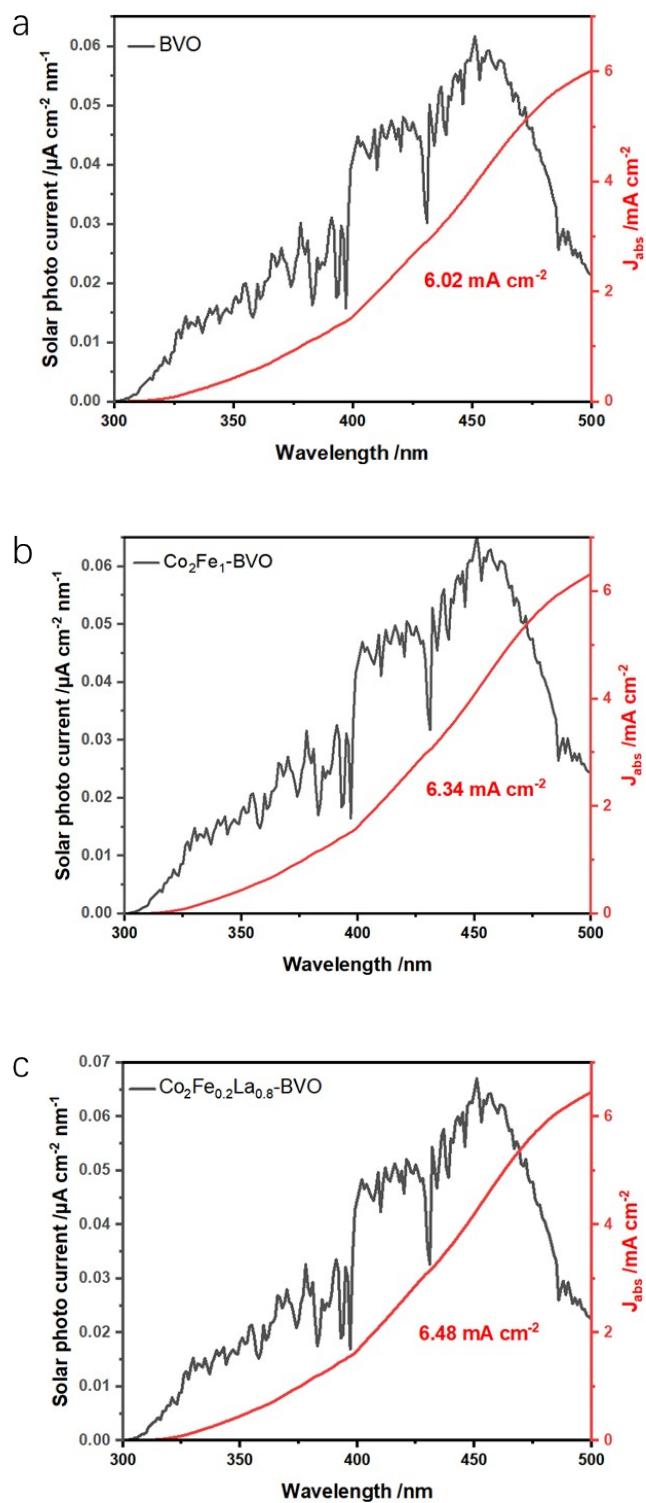
Fig. S13 Estimated solar photocurrent and integrated photocurrent of (a) $BiVO_4$, (b) Co_2Fe_1-LDHs/$BiVO_4$, and (c) $Co_2Fe_{0.2}La_{0.8}$-LDHs/$BiVO_4$.
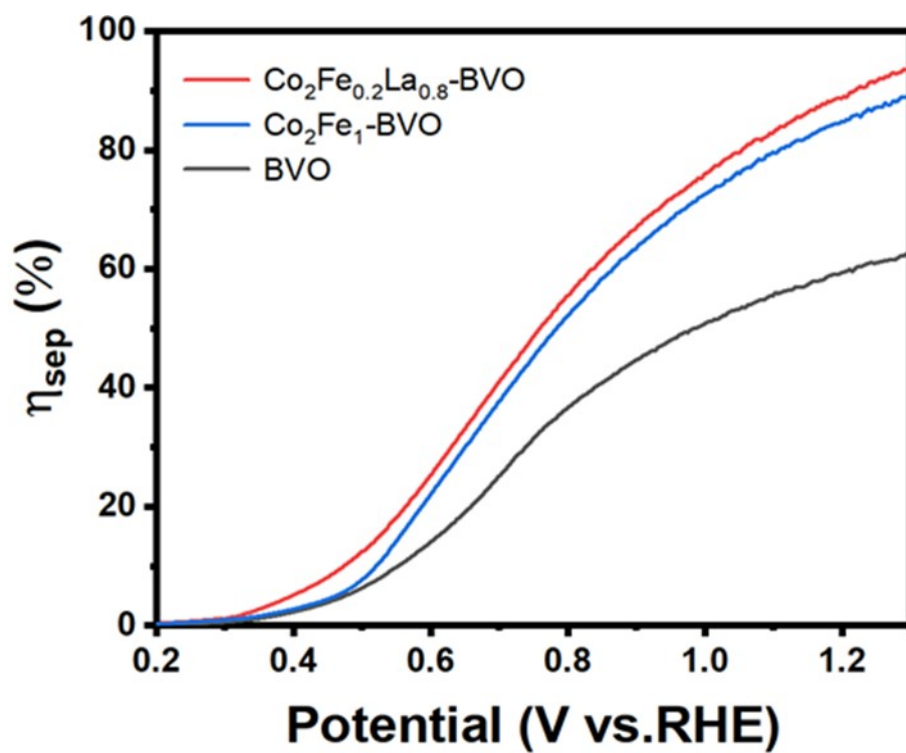
Fig. S14 Charge separation efficiencies $BiVO_4$, Co_2Fe_1-LDHs/$BiVO_4$ and $Co_2Fe_{0.2}La_{0.8}$-LDHs/$BiVO_4$.
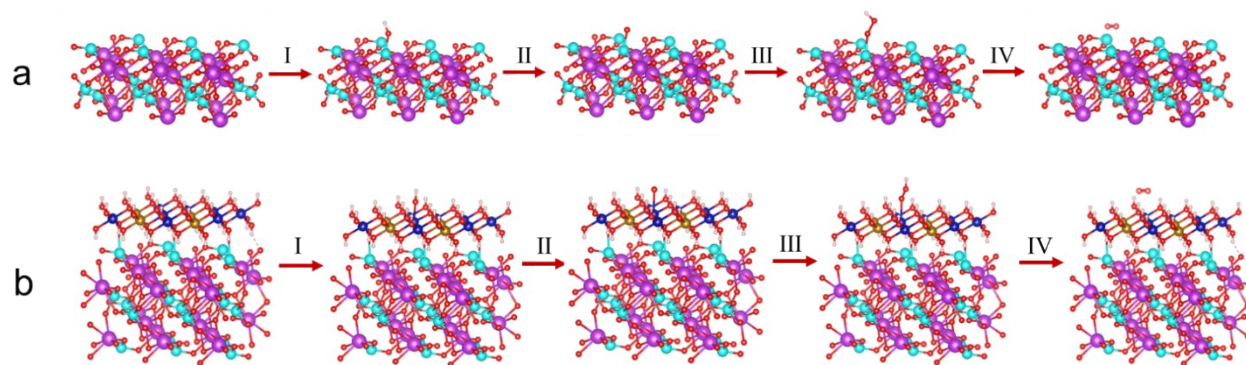
Fig. S15 Reaction steps of (a) $BiVO_4$ and (b) Co_2Fe_1-$BiVO_4$ with Co elements as active sites.

Table S1. The relative proportions of Fe^{3+} and Fe^{2+} in Co_2Fe_1-LDHs/$BiVO_4$ and $Co_2Fe_{0.2}La_{0.8}$-LDHs/$BiVO_4$.

Photoanodes	Peak area of Fe^{3+}	Peak area of Fe^{2+}	Relative ratio of Fe^{3+}/Fe^{2+}
Co_2Fe_1-$BiVO_4$	35251	44247	0.797
$Co_2Fe_{0.2}La_{0.8}$-$BiVO_4$	49750	33801	1.470

Table S2. The relative proportions of Co^{3+} and Co^{2+} in Co_2Fe_1-LDHs/$BiVO_4$ and $Co_2Fe_{0.2}La_{0.8}$-LDHs/$BiVO_4$.

Photoanodes	Peak area of Co^{3+}	Peak area of Co^{2+}	Relative ratio of Co^{3+}/Co^{2+}
Co_2Fe_1-$BiVO_4$	17502	19892	0.880
$Co_2Fe_{0.2}La_{0.8}$-$BiVO_4$	17639	14141	1.240

Table S3. The relative proportions of $BiVO_4$, Co_2Fe_1-LDHs/$BiVO_4$ and $Co_2Fe_{0.2}La_{0.8}$-LDHs/$BiVO_4$.

Photoanode	Peak area of lattice oxygen (O_L)	Peak area of oxygen vacancy (O_V)	Relative ratio of O_V/O_L
$BiVO_4$	145663.9	50861.21	0.349
Co_2Fe_1-$BiVO_4$	123756.07	77179.26	0.624
$Co_2Fe_{0.2}La_{0.8}$-$BiVO_4$	97817.86	110807.1	1.133

Table S4. Nd of $BiVO_4$, Co_2Fe_1-LDHs/$BiVO_4$ and $Co_2Fe_xLa_{1-x}$-LDHs/$BiVO_4$.

Photoanode	Nd/10^{18} cm^{-3}
$BiVO_4$	6.1
Co_2Fe_1-LDHs/$BiVO_4$	9.5
$Co_2Fe_{0.8}La_{0.2}$/$BiVO_4$	5.7
$Co_2Fe_{0.5}La_{0.5}$/$BiVO_4$	3.5
$Co_2Fe_{0.2}La_{0.8}$/$BiVO_4$	7.9
$Co_2Fe_{0.1}La_{0.9}$/$BiVO_4$	11.0

Table S5. Comparison of photo-electrochemical performance on $BiVO_4$-based photocatalysts.

Photo-catalyst	Current density under 1.23 V vs. RHE / mA cm^{-2}	Reference
$LaCo(OH)_x$/$BiVO_4$	2.02	7
Co/La $BiVO_4$	3.65	8
NiFe-LDH/F-$BiVO_4$	2.67	9
La0.3Co0.1Ce0.6/$BiVO_4$	3	10
$Co_2Fe_{0.2}La_{0.8}$-LDHs/$BiVO_4$	5.8	**This work**

Table S6. The R_s and R_{ct} values of sample $BiVO_4$, Co_2Fe_1-LDHs/$BiVO_4$, and $Co_2Fe_{0.2}La_{0.8}$-LDHs/$BiVO_4$

Sample	R_s (Ω)	R_{ct} (kΩ)
$BiVO_4$	11.25	18.45
Co_2Fe_1-LDHs/$BiVO_4$	9.39	6.53
$Co_2Fe_{0.2}La_{0.8}$-LDHs/$BiVO_4$	10.88	1.13

Table S7. The energy barriers of each OER pathway.

	U (V)	Step 1	Step 2	Step 3	Step 4
$BiVO_4$	0	0.89	0.93	2.11	0.99
	1.23	-0.34	-0.30	0.88	-0.24
Co_2Fe_1/$BiVO_4$	0	1.12	1.30	1.80	0.70
	1.23	-0.11	0.07	0.57	-0.53
$Co_2Fe_{0.2}La_{0.8}$/$BiVO_4$	0	0.51	1.52	1.66	1.23
	1.23	-0.72	0.29	0.43	0

References

[1] Kresse, G.; Furthmüller, J. Efficiency of Ab-Initio Total Energy Calculations for Metals and Semiconductors Using a Plane-Wave Basis Set. Comput. Mater. Sci. 6 (1996) 15−50.

[2] Kresse, G.; Furthmüller, J. Efficient Iterative Schemes for Ab initio Total-Energy Calculations Using a Plane-Wave Basis Set. Phys. Rev. B 54 (1996) 11169−11186.

[3] Perdew, J. P.; Burke, K.; Ernzerhof, M. Generalized Gradient Approximation Made Simple. Phys. Rev. Lett. 77 (1996) 3865−3868.

[4] Kresse, G.; Joubert, D. From ultrasoft pseudopotentials to the Projector Augmented-Wave Method. Phys. Rev. B 59 (1999) 1758-1775.

[5] Blöchl, P. E. Projector Augmented-Wave Method. Phys. Rev. B 50 (1994) 17953−17979.

[6] Henkelman, G.; Uberuaga, B. P.; Jonsson, H. A Climbing Image Nudged Elastic Band Method for Finding Saddle Points and Minimum Energy. Paths J. Chem. Phys. 113 (2000) 9901.

[7] Chhetri M, Dey S, Rao C N R. Photoelectrochemical Oxygen Evolution Reaction Activity of Amorphous Co–La Double Hydroxide-$BiVO_4$ Fabricated by Pulse Plating Electrodeposition. ACS Energy Lett. 2 (2017) 1062-1069.

[8] Geng H, Huang S, Kong D, *et al.* A novel synergy of Co/La Co-Doped Porous $Bivo_4$ Photoanodes with Enhanced Photoelectrochemical Solar Water Splitting Performance. J. Alloys Compd. 925 (2022) 166667.

[9] Liu J, Li J, Li Y, *et al.* Photoelectrochemical Water Splitting Coupled with Degradation of Organic Pollutants Enhanced by Surface and Interface Engineering of BiVO$_4$ Photoanode. Appl. Catal. B, 278 (2020) 119268.

[10] Guevarra D, Shinde A, Suram S K, *et al.* Development of Solar Fuels Photoanodes through Combinatorial Integration of Ni–La–Co–Ce Oxide Catalysts on BiVO$_4$. Energy Environ. Sci. 9 (2016) 565-580.